

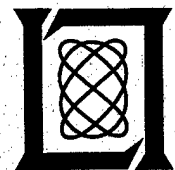
**Technical Report
1054**

A State-Space Technique for Ultrawide- Bandwidth Coherent Processing

**J.E. Piou
K.M. Cuomo
J.T. Mayhan**

20 July 1999

Lincoln Laboratory
MASSACHUSETTS INSTITUTE OF TECHNOLOGY
LEXINGTON, MASSACHUSETTS



Prepared for the Departments of the Air Force and Army
under Air Force Contract F19628-95-C-0002.

Approved for public release; distribution is unlimited.

DTIC QUALITY INSPECTED 4

19990729 029


This report is based on studies performed at Lincoln Laboratory, a center for research operated by Massachusetts Institute of Technology. This work was sponsored by the Department of the Air Force, NAIC, and the Department of the Army, USASMDC, under Air Force Contract F19628-95-C-0002.

This report may be reproduced to satisfy needs of U.S. Government agencies.

The ESC Public Affairs Office has reviewed this report, and it is releasable to the National Technical Information Service, where it will be available to the general public, including foreign nationals.

This technical report has been reviewed and is approved for publication.

FOR THE COMMANDER


Gary Tutungian
Administrative Contracting Officer
Contracted Support Management

Non-Lincoln Recipients

PLEASE DO NOT RETURN

Permission is given to destroy this document
when it is no longer needed.

MASSACHUSETTS INSTITUTE OF TECHNOLOGY
LINCOLN LABORATORY

**A STATE-SPACE TECHNIQUE FOR ULTRAWIDE-BANDWIDTH
COHERENT PROCESSING**

*J.E. PIOUS
K.M. CUOMO
J.T. MAYHAN
Group 34*

TECHNICAL REPORT 1054

20 JULY 1999

Approved for public release; distribution is unlimited.

ABSTRACT

A scheme is presented for estimating the ultrawide-bandwidth position and typing of scattering centers on a target using sparse-band measurements. The algorithm determines a set of matrices that best describe the measured data, then the fitted data are used to interpolate between and extrapolate outside of the measurement bands. A modal decomposition approach is used to estimate the position and typing of the scatterers. Standard pulse-compression techniques are applied to obtain a highly defined range profile of the target; application of these techniques is followed by extended coherent processing to generate superresolved two-dimensional images. The effectiveness of the new algorithm is confirmed by computer simulations; it is tested further using static-range data on a canonical test object.

TABLE OF CONTENTS

Abstract	iii
List of Illustrations	vii
List of Tables	ix
1. INTRODUCTION	1
2. SINGLE-BAND STATE-SPACE FORMULATION	3
2.1 Data Formulation	3
2.2 Transfer Function of the ARMA Model	3
2.3 State-Space Representation	4
2.4 State-Space Identification	6
3. SINGLE-BAND MODAL DECOMPOSITION AND STATE-SPACE EXTRAPOLATION	13
3.1 Overview	13
3.2 Simulated and Static-Range Examples	16
4. SPARSE-BAND STATE-SPACE FORMULATION	25
4.1 Sparse-Band Representation	25
4.2 Sparse-Band Identification Matrices	25
4.3 Simulated and Static-Range Examples	28
4.4 Iterative Method for State-Space Estimation and Interpolation	36
5. CONCLUSIONS	41
References	43

LIST OF ILLUSTRATIONS

Figure No.		Page
1	Comparison of the fitted model and the truth data for a four-point target for 200 independent trials with SNR = 40 dB for each run.	17
2	BWE of a four-point target for 200 independent trials with SNR = 40 dB for each run.	18
3	Comparison of the fitted model with truth data for a four-point target for 200 independent trials with SNR = 20 dB for each run.	19
4	BWE of a four-point target for 200 independent trials with SNR = 20 dB for each run.	20
5	Test target for UWB processing experiments, a monoconic model of a reentry vehicle 1.6 m long, with a spherical nosetip of 0.22-cm radius.	21
6	Static-range data of a monoconic target at 20-deg aspect for the I channel and Q channel.	21
7	Comparison of the extrapolated data from a 2.0-GHz-wide (14.0 to 16.0 GHz) data set and the true data for a monoconic reentry vehicle at 20-deg aspect.	22
8	Comparison of the extrapolated data from a 1.0-GHz-wide (14.5 to 15.5 GHz) data set and true data for the monoconic reentry vehicle at 20-deg aspect.	23
9	Average data samples for 200 independent trials of a four-point target with SNR = 20 dB for each run.	28
10	Comparison of the average of 200 independent trials for the lower-band extrapolations and truth data for a four-point target with SNR = 40 dB for each run.	29
11	Comparison of the average of 200 independent trials for the upper-band extrapolations and truth data for a four-point target with SNR = 40 dB for each run.	30
12	Comparison of the average of 200 independent trials of the UWB fitted model and truth data for a four-point target with SNR = 20 dB for each run.	31
13	Average data samples for 200 independent trials of a four-point target with SNR = 40 dB for each run.	33
14	Comparison of the average of 200 independent trials of the UWB fitted model and truth data for a four-point target with SNR = 40 dB for each run.	34
15	Sparse-band measurements used to predict a monoconic reentry vehicle's response over the full band from 12 to 18 GHz, and compressed pulses for the sparse- and full-band data sets.	35
16	Comparison of full-band data and the sparse-band model for a monoconic reentry vehicle at 20-deg aspect for the I channel and compressed pulses.	35
17	Comparison of the iterative UWB target response and full-band radar measurements for a monoconic reentry vehicle at 20-deg aspect for the I channel and compressed pulses.	37

LIST OF ILLUSTRATIONS (Continued)

Figure No.		Page
18	Iterative UWB eigenvalue estimates obtained using the sparse-band data sets illustrated in Figure 15(a).	37
19	Moment-method RCS calculations for the three major grooves on the monoconic reentry vehicle, which was at a 20-deg aspect angle.	38
20	Comparison of two-dimensional radar images.	39

LIST OF TABLES

Table No.		Page
1	Signal Parameters	16
2	Average Estimates of Signal Parameters for 200 Trials Conducted for Example 1 (SNR = 40 dB)	17
3	Average Estimates of Signal Parameters for 200 Trials Conducted for Example 2 (SNR = 20 dB)	19
4	Average Estimates of Signal Parameters Over 200 Trials Conducted for Example 5, Lower-Band (SNR = 20 dB)	29
5	Average Estimates of Signal Parameters Over 200 Trials Conducted for Example 5, Upper-Band (SNR = 20 dB)	31
6	Average Estimates of Signal Parameters over 200 Trials Conducted for Example 5, Sparse-Band (SNR = 20 dB)	32
7	Average Estimates of Signal Parameters for 200 Trials Conducted for Example 6, Sparse-Band (SNR = 40 dB)	33

1. INTRODUCTION

In 1990 Cuomo and others [1, 2] developed a bandwidth extrapolation (BWE) technique that allows the prediction of data samples that lie outside wideband radar measurements. The potential for BWE to resolve closely spaced scattering centers or to enhance the features on a target buried in noise has been demonstrated [1, 2]. For radar applications BWE improves the range resolution of compressed radar pulses by a factor of two to three. Although BWE demonstrably improves range resolution, the technique has inherent drawbacks. It is based on the assumption that radar returns from a complex target may be represented by a collection of point scatterers, each point scatterer having a constant amplitude over the range of frequencies under consideration; however, the constant-amplitude pointlike signal-processing model that characterizes BWE is sufficient only for wideband radars in which the bandwidth is small compared with the center frequency. Over ultrawide frequency bands, where the radar bandwidth is comparable with the center frequency, the amplitude of each scattering center may vary as a function of frequency. Physical scatterers such as spheres, edges, flat plates, and surface joints exhibit significant amplitude variations as a function of frequency [3]; therefore, ultrawide-bandwidth (UWB) signal models must be robust enough to describe this more general scattering behavior.

At sufficiently high frequencies UWB radar data may be modeled by a sum of damped sinusoids. From this damped sinusoid (or more precisely, a set of such sinusoids) the time delay and decay/growth are crucial to determining the position and typing of each scatterer embedded in a data set; the wider the bandwidth of the observation data set, the more precisely these typing parameters can be determined. Cost and hardware limitations are major drawbacks in building true UWB radars; to achieve potential UWB radar resolution, a UWB coherent-processing technique has been proposed in [4] to coherently combine sparse-band data obtained from, for example, a set of independently-operating conventional wideband sensors. The technique is based on an autoregressive (AR) signal model that does not consider the zeros of the transfer function that describes a radar return; in practice, using the AR signal model often limits the accuracy of the estimate of the sinusoid-damping factor.

This report presents a state-space technique for single- and sparse-band data, with the latter defined as state-space UWB processing. Unlike the UWB processing described in [4], state-space UWB processing is based on an autoregressive moving average (ARMA) that provides an enhanced sinusoid-damping factor and a better representation of UWB radar returns. The UWB processing proposed here uses the poles and zeros of the transfer function that best describes a radar return.

The remainder of this report is organized as follows. Section 2 presents a mathematical model for damped signals and describes the single-band state-space technique. Section 3 describes mathematical expressions for the signal parameters and presents simulated and static-range experiments to estimate the signal parameters and predict the data samples that lie outside the measurement band. The so-called state-space UWB technique is presented in Section 4, with radar-imaging examples included to demonstrate the practicability of the method. The conclusions of the study are presented in Section 5.

2. SINGLE-BAND STATE-SPACE FORMULATION

2.1 DATA FORMULATION

This subsection considers the data sequence $y(k)$ that comprises uniformly spaced samples of p complex sinusoids corrupted by white noise $w(k)$. Signal measurements at N frequencies may be modeled as

$$y(k) = \sum_{i=1}^P a_i e^{-(\alpha_i + j2\pi\tau_i)f_k} + w(k) \quad ; \quad k = 1, \dots, N \quad , \quad (1)$$

where a_i and α_i denote the amplitude and decay/growth associated with the i^{th} scattering center, respectively. The parameter τ_i denotes the time delay of the i^{th} scatterer, which is related to the range parameter r_i by $\tau_i = (2r_i)/c$, where c is the speed of light. The k^{th} element of the frequency vector is related to the carrier frequency f_1 by $f_k = f_1 + (k-1)\Delta f$, where Δf is the sampling frequency. In this report the primary interest is in estimating the parameters embedded in the data sequence $y(k)$. In the state-space method the decay/growth and time-delay parameters can be easily computed from the eigenvalues of an open-loop matrix. Once these parameters are accurately estimated, the amplitudes a_i can readily be derived from the state-space matrices using a modal decomposition method. The state-space formulation for the single and dual bands that are studied in detail in this report may be seen as an input-output relationship between the noise $w(k)$ and the data sequence $y(k)$. The best way to derive the state-space matrices is to rewrite Equation (1) as a difference equation and study its transfer function. The next subsection presents the difference equation that best describes the input-output relationship between $y(k)$ and $w(k)$ and that allows the state-space formulation for the single band.

2.2 TRANSFER FUNCTION OF THE ARMA MODEL

The input-output relationship for the general ARMA is given by the difference equation

$$y(k) = \sum_{i=1}^m d_i y(k-i) + \sum_{j=1}^q b_j w(k-j) + b_0 w(k) \quad , \quad (2)$$

where $w(k)$ and $y(k)$ are the input and output, respectively. The transfer function $H(z)$ of the system described by Equation (1) may be defined by

$$H(z) = \frac{Y(z)}{W(z)} = \frac{B_0(z)}{A_0(z)} \quad , \quad (3)$$

where

$$A_0(z) = 1 - \sum_{i=1}^m d_i z^{-i} \quad (4)$$

and

$$B_0(z) = b_0 + \sum_{j=1}^q b_j z^{-j} \quad (5)$$

The roots of the polynomial $A_0(z)$ are the poles of the system; the roots of $B_0(z)$ determine the zeros. An interesting and popular special case of the ARMA model that is described by Equation (2) is the AR model. The input-output relationship for the AR model may be written as

$$y(k) = \sum_{i=1}^m d_i y(k-i) + b_0 w(k) \quad (6)$$

The transfer function of the AR model is therefore given by

$$H(z) = \frac{b_0}{A_0(z)} \quad (7)$$

where $A_0(z)$ is defined by Equation (4). As the AR model is a special case of the ARMA, the state-space representation will be carried out on the ARMA model in this report, unless specified otherwise. The next subsection presents the state-space method for the ARMA model.

2.3 STATE-SPACE REPRESENTATION

State-space signal modeling provides an alternative representation of a linear-rational system that is popular in linear system and control theory. In this formulation the input-output description of the ARMA model, instead of being given by Equation (1), is given by the state-space equations

$$x(k+1) = Ax(k) + Bw(k) \quad (8)$$

and

$$y(k) = Cx(k) + w(k) \quad (9)$$

where $x(k) \in \mathbf{R}^{p \times 1}$ is the state and $A \in \mathbf{R}^{p \times p}$, $B \in \mathbf{R}^{p \times 1}$, and $C \in \mathbf{R}^{1 \times p}$ are constant matrices. The transfer function of the state-space formulation is obtained by taking the z -transform of Equations (8) and (9) and evaluating the ratio $Y(z)$ to $W(z)$ as follows:

$$X(z) = (zI - A)^{-1}BW(z) \quad (10)$$

and

$$Y(z) = CX(z) + W(z) \quad (11)$$

Inserting Equation (10) into Equation (11) obtains

$$Y(z) = C(zI - A)^{-1}BW(z) + W(z) \quad ; \quad (12)$$

thus,

$$H(z) = C(zI - A)^{-1}B + 1 \quad , \quad (13)$$

where I is an identity matrix. Equation (13) shows that the ARMA model for a discrete-time process $y(k)$ in state-space notation is related to the transfer function such that the poles of the model [i.e., the roots of the polynomial $A_0(z)$, which is defined by Equation (4)] are the eigenvalues of the open-loop matrix A . Furthermore, the zeros [i.e., the roots of $B_0(z)$, which is given by Equation (5)] are the eigenvalues of the matrix $(A - BC)$. The transfer function for a given system is unique; however, the triplet (A, B, C) depends on the transformation that gives rise to the transfer function. Generally speaking, for a given transfer function the triplet (A, B, C) of a minimal realization is a unique modulo of a similarity coordinate transformation. Interesting choices of coordinates lead to canonical or companion forms; one of these forms is the left canonical, where the open-loop matrix A is given by

$$A = \begin{bmatrix} d_1 & 1 & 0 & \dots & 0 \\ d_2 & 0 & 1 & \dots & 0 \\ \vdots & \vdots & \vdots & \ddots & \vdots \\ \vdots & \vdots & \vdots & \dots & \vdots \\ \vdots & \vdots & \vdots & \vdots & \vdots \\ d_{m-1} & 0 & 0 & \dots & 1 \\ d_m & 0 & 0 & \dots & 0 \end{bmatrix} \quad , \quad (14)$$

where the values for d_i are given by Equation (4). This form directly relates the state-space model to the transfer function parameters. The matrices B and C may also be derived from the left-canonical form; interested readers are referred to [5]. Besides the companion forms, the state-space matrices may also be derived from information embedded in the data vector throughout an impulse-response sequence. The following subsection gives a procedure for estimating the triplet (A, B, C) from a given data vector.

2.4 STATE-SPACE IDENTIFICATION

Let the impulse response of the ARMA model be represented by Equation (13). To identify the state-space matrices (A, B, C) from the impulse response, the matrix $(zI - A)^{-1}$ is expanded into an infinite series. It can be shown that

$$(zI - A)^{-1} = Iz^{-1} + Az^{-2} + Az^{-3} + \dots \quad (15)$$

Inserting Equation (15) into Equation (13), one obtains

$$Y(z) = 1 + CBz^{-1} + CABz^{-2} + CA^2Bz^{-3} + \dots \quad (16)$$

Referring to the definition of the z -transform, Equation (16) may be written as

$$Y(z) = y(0) + y(1)z^{-1} + y(2)z^{-2} + \dots + y(k)z^{-k} + \dots \quad (17)$$

By comparing the coefficients of the z^{-k} terms of Equations (16) and (17), the following sequence is obtained:

$$y(0) = 1 \quad (18)$$

$$y(1) = CB \quad (19)$$

$$y(2) = CAB \quad (20)$$

$$\begin{aligned} & \cdot \\ & \cdot \\ & \cdot \\ y(k) &= CA^{k-1}B \quad (21) \\ & \cdot \\ & \cdot \end{aligned}$$

Then the relationship between the impulse response of the model and the state-space parameters for any positive value of k is defined by

$$y(k) = CA^{k-1}B \quad (22)$$

Equation (22) indicates that a Hankel matrix H formed from an impulse-response sequence such that

$$H = \begin{bmatrix} y(1) & y(2) & y(3) & \dots \\ y(2) & y(3) & y(4) & \dots \\ y(3) & y(4) & y(5) & \dots \\ \cdot & \cdot & \cdot & \cdot \\ \cdot & \cdot & \cdot & \cdot \\ \cdot & \cdot & \cdot & \cdot \end{bmatrix} \quad (23)$$

can be factored. The decomposition of H into a product of two matrices is given by

$$H = \begin{bmatrix} C \\ CA \\ CA^2 \\ \cdot \\ \cdot \\ \cdot \end{bmatrix} \begin{bmatrix} B & AB & A^2B & \dots \end{bmatrix}, \quad (24)$$

or equivalently,

$$H = \Omega \Gamma, \text{ where} \quad (25)$$

$$\Omega = \begin{bmatrix} C \\ CA \\ CA^2 \\ \cdot \\ \cdot \\ \cdot \end{bmatrix} \quad (26)$$

and

$$\Gamma = \begin{bmatrix} B & AB & A^2B & \dots \end{bmatrix}. \quad (27)$$

In linear system theory Ω and Γ are known as the observability and controllability matrices. Despite the infinite dimensions of H [which is defined by Equation (23)], Ω and Γ can be truncated to p columns and p rows, respectively. Consequently, H has finite rank $r \leq p$. For a given set of measurements the Hankel matrix H is, of course, always finite. In this case H may be considered to be an operator constructed from a set of measurements $y(k)$ that maps the past input vector w^- to the future output y^+ . In the remaining portion of this subsection a method is proposed to compute the Hankel matrix, together with a scheme to derive the state-space matrices from a finite set of samples.

Let a set of measurements be defined by

$$y = [y(1) y(2) y(3) \dots y(N)] \quad (28)$$

and assume that it is desirable to derive the corresponding state-space matrices. The first step in computing the triplet (A, B, C) is to form the Hankel matrix from the available data samples. Therefore

$$H = \begin{bmatrix} y(1) & y(2) & y(3) & \dots & y(L) \\ y(2) & y(3) & y(4) & \dots & y(L+1) \\ \vdots & \vdots & \vdots & \dots & \vdots \\ \vdots & \vdots & \vdots & \dots & \vdots \\ y(N-L) & y(N-L+1) & y(N-L+2) & \dots & y(N-1) \\ y(N-L+1) & y(N-L+2) & y(N-L+3) & \dots & y(N) \end{bmatrix}, \quad (29)$$

where the correlation window length $L = (2N/3)$ is the smallest integer $\leq (2N/3)$. The Hankel matrix given in Equation (29) may be partitioned into signal and noise subspaces by means of a singular-value decomposition. Computing the singular-value decomposition of H and rearranging its singular values $\{\sigma_i\}$ in decreasing order gives

$$H = \begin{bmatrix} U_{sn} & U_n \end{bmatrix} \begin{bmatrix} \Sigma_{sn} & 0 \\ 0 & \Sigma_n \end{bmatrix} \begin{bmatrix} V_{sn}^* \\ V_n^* \end{bmatrix}, \quad (30)$$

where the subscripts sn and n denote the signal and noise subspaces, respectively, and the asterisk refers to conjugate and transpose. The matrices U_{sn} and U_n are the signal and noise components of the left-unitary matrix $\begin{bmatrix} U_{sn} & U_n \end{bmatrix}$, respectively. Further, V_{sn} and V_n , respectively, denote the signal and noise components of the right-unitary matrix $\begin{bmatrix} V_{sn} & V_n \end{bmatrix}$, and Σ_{sn} and Σ_n are diagonal matrices with the signal and noise singular values as entries on their main diagonal, respectively. To increase the accuracy of the state-space matrices, the Hankel matrix H may be truncated by suppressing the noise-singular values and their associated unitary matrix components. It is well known that a p -rank matrix that best approximates Equation (30) in the spectral norm sense is obtained by retaining only the dominant components, i.e.,

$$\tilde{H} = U_{sn} \Sigma_{sn} V_{sn}^* \quad (31)$$

The approximation of the error between H and \tilde{H} in the spectral norm sense is given by

$$\sigma_{p+1} = \|H - \tilde{H}\|_s, \quad (32)$$

where the subscript s denotes spectral. Therefore if σ_p is very large with respect to σ_{p+1} , \tilde{H} is a good approximation for H ; moreover, \tilde{H} is obtained in factored form by

$$\tilde{H} = U_{sn} \Sigma_{sn} V_{sn}^* = \tilde{\Omega} \tilde{\Gamma} \quad (33)$$

The observability and controllability matrices $\tilde{\Omega}$ and $\tilde{\Gamma}$ may be computed from Equation (33). By using the balanced coordinate method proposed in [6], the observability and controllability matrices are obtained by choosing

$$\tilde{\Omega} = U_{sn} \Sigma_{sn}^{1/2} \quad (34)$$

and

$$\tilde{\Gamma} = \Sigma_{sn}^{1/2} V_{sn}^* \quad (35)$$

respectively. Ideally $\tilde{\Omega}$ would have the exact observability matrix structure, and the open-loop matrix $A \in C^{P \times P}$ is the solution to the following matrix equation:

$$\tilde{\Omega}_{-r1} A = \tilde{\Omega}_{-r1} \quad (36)$$

where

$$\tilde{\Omega}_{-r1} = \begin{bmatrix} CA \\ CA^2 \\ CA^3 \\ \vdots \\ CA^{N-L} \end{bmatrix} \quad (37)$$

and

$$\tilde{\Omega}_{-rl} = \begin{bmatrix} C \\ CA \\ CA^2 \\ \vdots \\ CA^{N-L-1} \end{bmatrix} \quad (38)$$

The matrices $\tilde{\Omega}_{-r1}$ and $\tilde{\Omega}_{-rl}$ are obtained by deleting the first and last rows of the observability matrix $\tilde{\Omega}$, respectively. From Equation (36) the following open-loop matrix is then obtained:

$$A = (\tilde{\Omega}_{-r}^* \tilde{\Omega}_{-r})^{-1} \tilde{\Omega}_{-r}^* \tilde{\Omega}_{-r-1} \quad , \quad (39)$$

The open-loop matrix defined by Equation (39) may also be derived from the controllability matrix $\tilde{\Gamma}$. It is not difficult to see that A satisfies

$$A\tilde{\Gamma}_{-cl} = \tilde{\Gamma}_{-c1} \quad , \quad (40)$$

where

$$\tilde{\Gamma}_{-cl} = \begin{bmatrix} B & AB & A^2B & \dots & A^{L-2}B \end{bmatrix} \quad (41)$$

and

$$\tilde{\Gamma}_{-c1} = \begin{bmatrix} AB & A^2B & A^3B & \dots & A^{L-1}B \end{bmatrix} \quad . \quad (42)$$

It is clear that Equations (41) and (42) are obtained by deleting the first and last columns, respectively, of the controllability matrix $\tilde{\Gamma}$ [which is defined by Equation (27)]. By solving for the open-loop matrix, Equation (40) gives, equivalently to Equation (39),

$$A = \tilde{\Gamma}_{-c1} \tilde{\Gamma}_{-cl}^* (\tilde{\Gamma}_{-cl} \tilde{\Gamma}_{-cl}^*)^{-1} \quad . \quad (43)$$

The state-space matrix C may next be computed from the observability matrix, which is described by Equation (26). Thus

$$C = \tilde{\Omega}(1, :) \quad . \quad (44)$$

From Equation (44) it is easy to see that C is the first row of $\tilde{\Omega}$. For the state-space impulse response to match the data vector y [which is given by Equation (28)], the matrix B must be computed by a least-squares method. To ease the least-squares computation of B , define a new controllability matrix by

$$\tilde{\Omega}_N = \begin{bmatrix} C \\ CA \\ CA^2 \\ \vdots \\ \vdots \\ CA^{N-1} \end{bmatrix} \quad , \quad (45)$$

where N is the number of samples. Then use the above equation, together with the matrix B , to match the data. Mathematically, then,

$$\tilde{\Omega}_N B = y^T \quad , \quad (46)$$

where y is the data vector and the superscript T denotes transpose. By using the pseudoinverse method, Equation (46) gives

$$B = (\tilde{\Omega}_N^* \tilde{\Omega}_N)^{-1} \tilde{\Omega}_N^* y^T \quad . \quad (47)$$

A similar equation to the one defined above can be derived for C . To compute C from the data set using a least-squares on a controllability matrix, B must be rewritten as

$$B = \tilde{\Gamma}(:, 1) \quad . \quad (48)$$

In this case it is clear that B is given by the first row of $\tilde{\Gamma}$. Now the new controllability matrix may be defined by

$$\tilde{\Gamma}_N = \begin{bmatrix} B & AB & A^2B & \dots & A^{N-1}B \end{bmatrix} \quad . \quad (49)$$

Next the state-space impulse response [which is defined by Equation (22)] is matched to the data. Mathematically this may be written as

$$C \tilde{\Gamma}_N = y \quad . \quad (50)$$

Finally, by using the pseudoinverse method, Equation (50) becomes

$$C = y \tilde{\Gamma}_N^* (\tilde{\Gamma}_N \tilde{\Gamma}_N^*)^{-1} \quad . \quad (51)$$

It is significant that two expressions for the open-loop matrix A may be computed from the observability matrix by using Equation (39) or from the controllability matrix by using Equation (43). When C is computed using Equation (44), B must be obtained from Equation (47); however, when C is computed from the above equation, B must be obtained from Equation (48).

The state-space method can be used to identify target features embedded in the data set for a finite length of measurements once the triplet (A, B, C) is defined. Furthermore, Equation (22) may be used to extrapolate the data beyond the band of observations. The next section presents a technique based on a modal decomposition approach that allows identification of target features and extrapolation of available data.

3. SINGLE-BAND MODAL DECOMPOSITION AND STATE-SPACE EXTRAPOLATION

3.1 OVERVIEW

Generally speaking, the modal decomposition approach may be defined as a transformation method that allows a new state-space representation of a linear system by keeping invariant the eigenvalues of the original system. This method is often referred to as the similarity transformation in control theory and may be described as follows.

Assume that the eigenvalues of A [which may be defined by Equation (39) or (43)] are distinct; thus,

$$\lambda\{A\} = [\lambda_1 \ \lambda_2 \ \dots \ \lambda_p] \quad (52)$$

It is well known that the eigenvalues (λ_i), which determine the decay/growth of the system output, and the eigenvectors (m_i), which give the shape of the response, satisfy

$$Am_i = \lambda_i m_i \quad ; \quad i = 1, \dots, p \quad (53)$$

Form with the p eigenvectors a modal matrix M such that

$$M = [m_1 \ m_2 \ \dots \ m_p] \quad (54)$$

It is then not difficult to see from Equations (52) through (54) that

$$AM = M\Lambda \quad , \quad (55)$$

where

$$\Lambda = \text{diag}[\lambda_1 \ \lambda_2 \ \dots \ \lambda_p] \quad (56)$$

Then suppose that

$$x(k) = Mz(k) \quad , \quad (57)$$

where $z(k)$ is the new state variable. Expressions equivalent to Equations (8) and (9) may be written as

$$z(k+1) = \Lambda z(k) + M^{-1}Bw(k) \quad (58)$$

and

$$y(k) = CMz(k) + w(k) \quad , \quad (59)$$

respectively. It is easy to see from Equation (55) that Λ is given by

$$\Lambda = M^{-1}AM \quad . \quad (60)$$

The entries on its main diagonal are exactly the eigenvalues of the open-loop matrix A ; therefore, the modal decomposition approach carries information that may characterize the target, and this seems to be a potential candidate for identifying scatterers embedded in the data set. The eigenvalues (λ_i) carry typing and position information about the target features. Their magnitudes and phases are related to the decay/growth and time-delay parameters by

$$\alpha_i = -\frac{\log|\lambda_i|}{\Delta f} \quad ; \quad i = 1, \dots, p \quad (61)$$

and

$$\tau_i = -\frac{\phi_i}{2\pi\Delta f} \quad ; \quad i = 1, \dots, p \quad , \quad (62)$$

respectively. In Equation (61) $||$ denotes the magnitude of the inserted variable and Δf is the sampling frequency; in Equation (62) ϕ_i refers to the phase of the eigenvalue (λ_i). By following the steps defined by Equations (16) through (21) and using the modal decomposition approach, the estimated samples may be written as

$$y(k) = CMA^{k-1}M^{-1}B \quad ; \quad k > 0 \quad . \quad (63)$$

The above equation is identical to Equation (22); it gives good estimates of the available samples, consistent with Equation (32). The amplitudes of the signals related to the scatterers may be derived from Equation (63) as follows.

Let

$$M^{-1} = \begin{bmatrix} v_1 \\ v_2 \\ \cdot \\ \cdot \\ \cdot \\ v_p \end{bmatrix} \quad . \quad (64)$$

Inserting Equations (54), (56), and (64) into Equation (63) obtains

$$y(k) = \sum_{i=1}^P (Cm_i)(v_i B) \lambda_i^{k-1} ; k = 1, \dots, N . \quad (65)$$

By using the signal model described by Equation (1), it is not difficult to see that the signal amplitudes are related to the state-space matrices by

$$a_i = \frac{(Cm_i)(v_i B)}{(\lambda_i)^{\Delta f} \frac{f_1}{\Delta f}} ; i = 1, \dots, P , \quad (66)$$

where f_1 and Δf denote the first frequency component of the frequency vector and the sampling frequency, respectively. As the signal parameters are accurately estimated, the state-space matrices can be used to extrapolate the data set to other frequency bands.

Suppose that the state-space model is used to extrapolate the available data set in the forward direction. The first N_1 extrapolated samples may be obtained by using

$$y_f(k) = CMA^{N+k-1}M^{-1}B ; k = 1, 2, \dots, N_1 , \quad (67)$$

or equivalently,

$$y_f(k) = CA^{N+k-1}B ; k = 1, 2, \dots, N_1 , \quad (68)$$

where f and N denote forward and the number of available samples, respectively. To extrapolate the data in the reverse direction, the state-space matrices A_r , B_r , and C_r may be derived from the flipped data $[y(N) \ y(N-1) \ \dots \ y(1)]$ and used in Equation (67). Thus the first N_1 backward-extrapolated samples may be written as

$$y_b(k) = C_r M_r \Lambda_r^{N+k-1} M_r^{-1} B_r ; k = 1, 2, \dots, N_1 , \quad (69)$$

or equivalently,

$$y_b(k) = C_r A_r^{N+k-1} B_r ; k = 1, 2, \dots, N_1 , \quad (70)$$

where b refers to backward, and M_r and Λ_r denote the modal and eigenvalue matrices of A_r . The modal approach of the backward-extrapolation equation that is defined by Equation (70) is a direct consequence of Equation (68); it is obtained by replacing the constant matrices Λ , M , B , and C of the forward extrapolation by Λ_r , M_r , B_r , and C_r , respectively. The state-space method is well suited for target identification and data extrapolation. The entries on the main diagonal of Λ or Λ_r carry information about the decay/growth and the range location of the scatterers, and Equation (67) or (68) can be used for data extrapolation.

To test the feasibility of the technique and judge its practicability, the state-space method will be applied to simulated and static-range radar data. The next subsection presents examples from simulated and static-range radar data in order to analyze the performance of the single-band algorithm.

3.2 SIMULATED AND STATIC-RANGE EXAMPLES

Examples from simulated and static-range radar data confirm the single-band state-space algorithm. In the simulated examples the targets are four-point scatterers. The measurement noise $w(k)$ is complex white Gaussian noise with variance, which is defined by peak signal-to-noise ratio (SNR):

$$SNR = 20 \log \left(\frac{\sigma_{sn}}{\sigma_n} \right) , \quad (71)$$

where σ_{sn}^2 denotes the signal variance. In the static-range example, the target is a monoconic model of a reentry vehicle with grooves, a slip-on ring, and seams.

3.2.1 Example 1 (Simulated)

The full-bandwidth synthetic data are generated using Equation (1) over the frequency range 3 to 10 GHz, with a sampling rate of 20.057 MHz. The SNR is 40 dB, and the signal parameters are defined in Table 1.

TABLE 1
Signal Parameters

Scattering Centers	Decay/Growth (α)	Time Delay (τ)	Amplitude ($ a $)
1st	-0.9231×10^{-9}	2×10^{-9}	1
2nd	-0.2308×10^{-9}	6×10^{-9}	1
3rd	-0.3077×10^{-9}	1×10^{-8}	1
4th	1×10^{-17}	14×10^{-9}	1

To test the feasibility of the algorithm, 200 independent trials were performed using the signal parameters defined above ($SNR = 40$ dB). For each trial the focus is on a segment of the data, with 101 samples in the frequency range 5.5 to 7.5 GHz. To estimate the signal parameters, Akaike's information criterion (AIC) [7] is used to identify the number of scattering centers. For each trial the AIC detects the four signals embedded in the data sets. Figures 1(a) and 1(b) show good agreement between the average of the estimates and the data for the in-phase (I) and quadrature (Q) channels, respectively. The average estimates of the signal parameters are given in Table 2. Figures 2(a) and 2(b) show the forward- and backward-extrapolation of the average estimates of the I and Q channels, respectively.

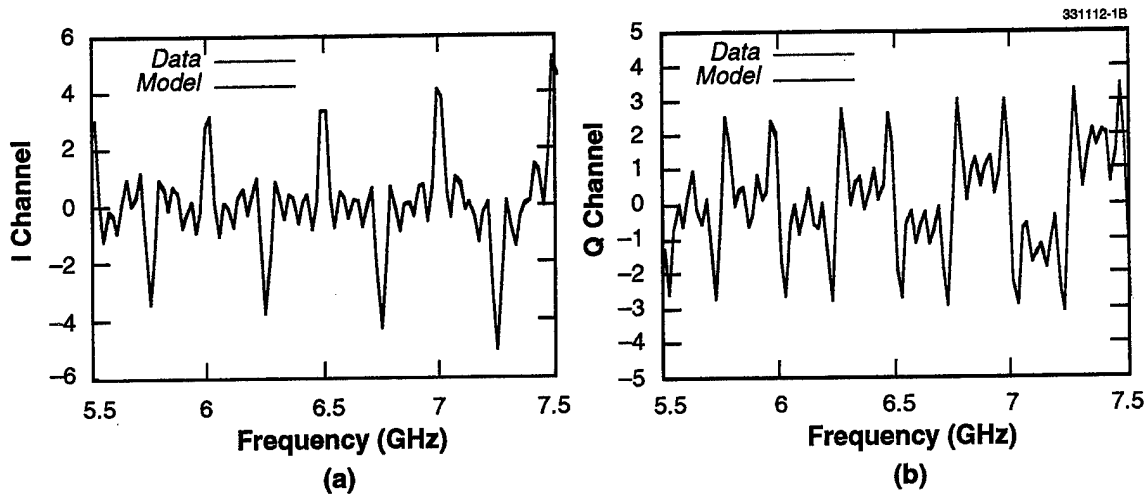


Figure 1. Comparison of the fitted model (blue) and the truth data (red) for a four-point target for 200 independent trials with SNR = 40 dB for each run. (a) Average of the I channels, and (b) average of the Q channels.

TABLE 2
Average Estimates of Signal Parameters for 200 Trials Conducted
for Example 1 (SNR = 40 dB)

Scattering Centers	Decay/Growth (α)		Time Delay (τ)		Amplitude ($ a $)	
	Estimates	% Error	Estimates	% Error	Estimates	% Error
1st	-0.9118×10^{-9}	1.22	1.98×10^{-9}	1.0	0.997	0.3
2nd	-0.2084×10^{-9}	9.71	5.8×10^{-9}	3.33	1.03	3.0
3rd	-0.3318×10^{-9}	7.83	1×10^{-8}	0	0.995	0.5
4th	0.51×10^{-16}	4.1	13.8×10^{-9}	1.43	1	0

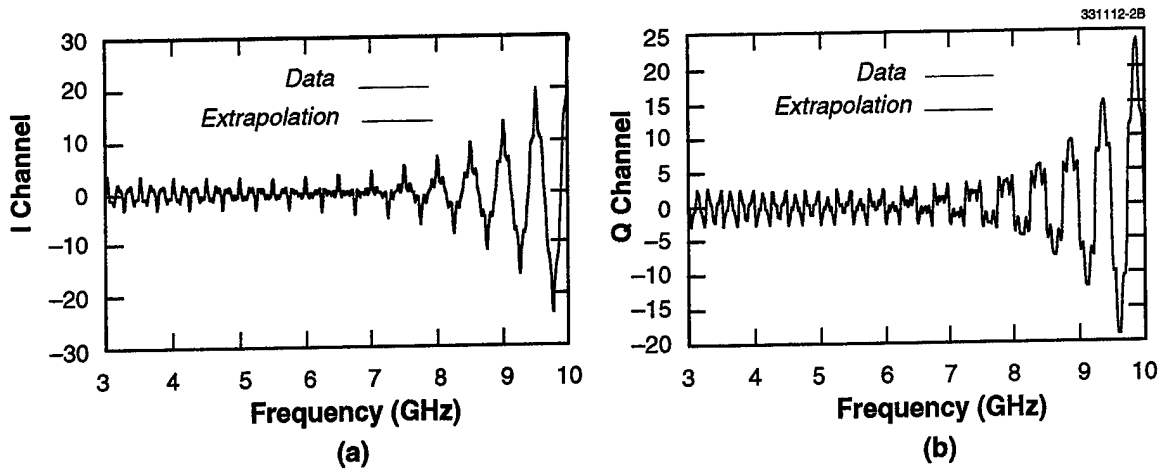


Figure 2. BWE (blue) of a four-point target for 200 independent trials with SNR = 40 dB for each run. (a) Average of the I channels, and (b) average of the Q channels.

3.2.2 Example 2 (Simulated)

Example 1 was repeated, decreasing the SNR to 20 dB. In each trial the AIC detects the four signals that are used to generate the data set. Figures 3(a) and 3(b) compare the average of the models and the data for the I and Q channels, respectively. The algorithm filters a great deal of noise, giving results that follow more closely a data set with higher SNR. Table 3 presents the average estimates of the signal parameters for 200 independent trials. The forward- and backward-extrapolation for the average of the I and Q channels are shown in Figures 4(a) and 4(b), respectively.

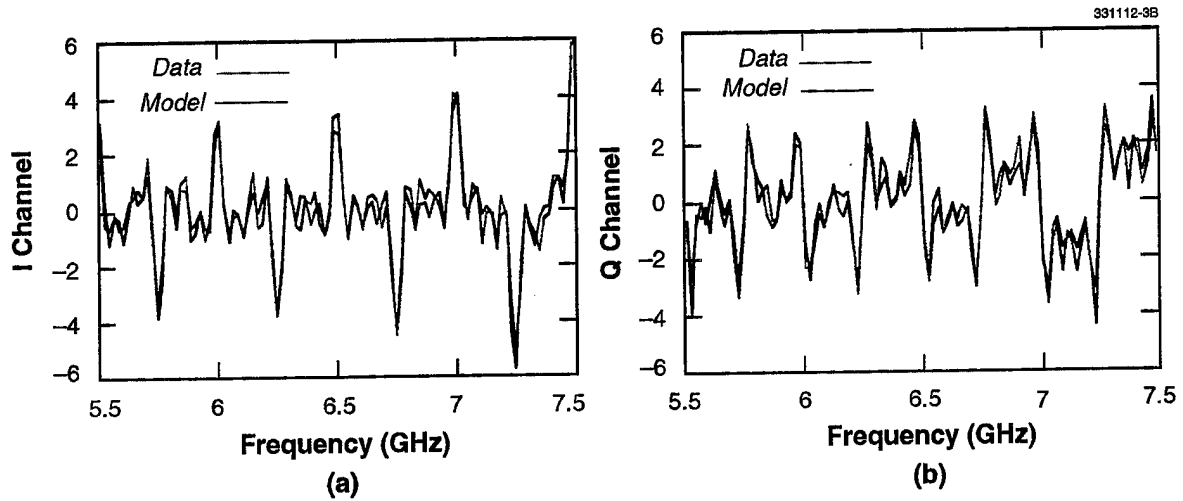


Figure 3. Comparison of the fitted model (blue) with truth data (red) for a four-point target for 200 independent trials with SNR = 20 dB for each run. (a) Average of the I channels, and (b) average of the Q channels.

TABLE 3
Average Estimates of Signal Parameters for 200 Trials Conducted
for Example 2 (SNR = 20 dB)

Scattering Centers	Decay/Growth (α)		Time Delay (τ)		Amplitude ($ a $)	
	Estimates	% Error	Estimates	% Error	Estimates	% Error
1st	-0.9182×10^{-9}	0.53	1.92×10^{-9}	4.0	0.934	6.6
2nd	-0.2073×10^{-9}	10.18	5.73×10^{-9}	4.5	1.11	11.0
3rd	-0.343×10^{-9}	11.47	1.17×10^{-8}	17.0	0.987	1.30
4th	0.87×10^{-16}	7.7	13.6×10^{-9}	2.86	1.04	4.0

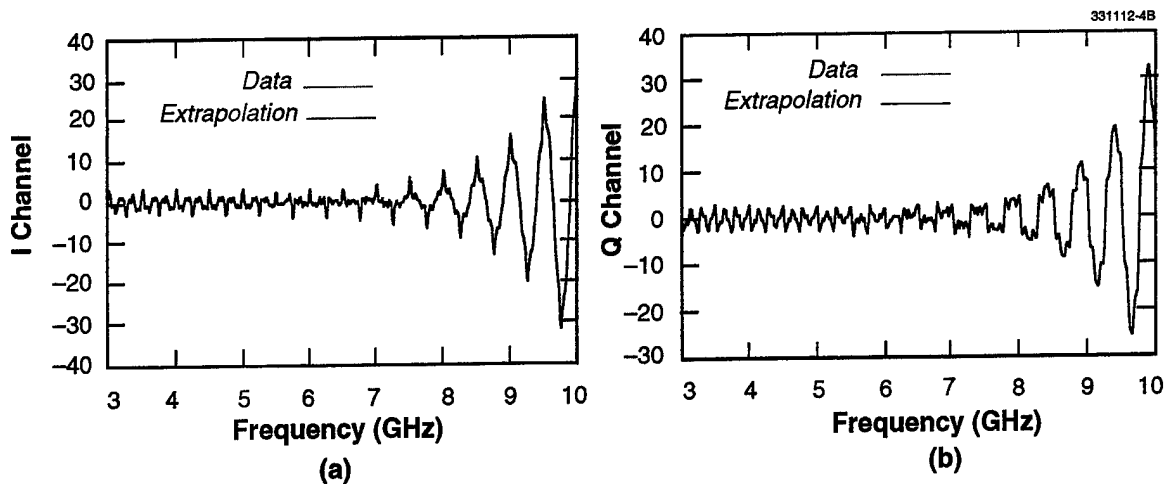


Figure 4. BWE (blue) of a four-point target for 200 independent trials with $SNR = 20$ dB for each run. (a) Average of the I channels, and (b) average of the Q channels.

3.2.3 Example 3 (Static-Range Radar Data)

Data were collected for this third experiment on the monoconic reentry vehicle, which is illustrated in Figure 5; for a complete description of the target, interested readers are referred to [4]. The data are very good quality, i.e., they have very high SNR. The measurements were taken from 4.64 to 18 GHz using a 40-MHz step size. The target viewing angles relative to nose-on ranged from -5 to 95 deg in 0.25 -deg increments.

Demonstration of the state-space processing technique considered a segment of a radar pulse in the 12- to 18-GHz range, corresponding to an aspect of 20 deg. To test the practicability of the algorithm, the radar pulse was reduced to a 2-GHz-wide band, as illustrated in Figures 6(a) and 6(b). Figures 7(a) and 7(b) show good agreement between the data and the state-space extrapolation for the I and Q channels. In practice, for an extrapolation interval roughly equal to the data band on either side, the predicted samples do not carry useful information when the extrapolation factor becomes large. This fact is due to the error that occurs in the estimate of the decay/growth parameter α . The strong dependence of the eigenvalue (λ) on α reflects the exponential decay or growth of the response outside the band of observation.

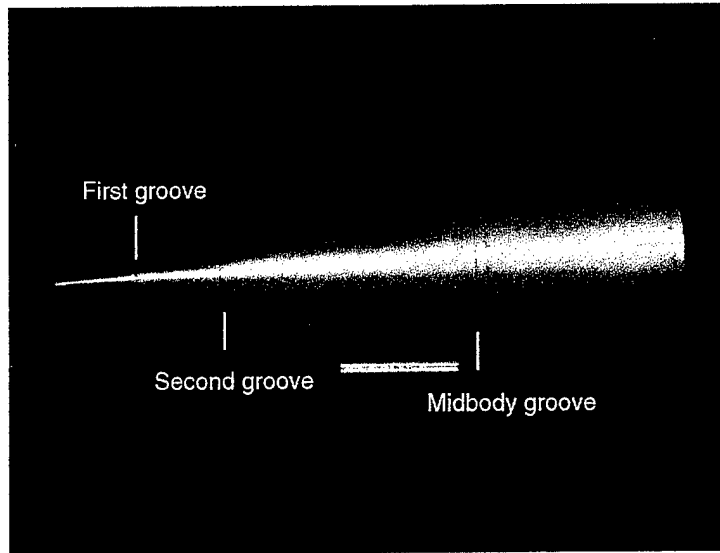


Figure 5. Test target for UWB processing experiments, a monoconic model of a reentry vehicle 1.6 m long, with a spherical nosetip of 0.22-cm radius. The nose section is made from a solid piece of machined aluminum with three grooves, two near the front of the model and one at the midbody.

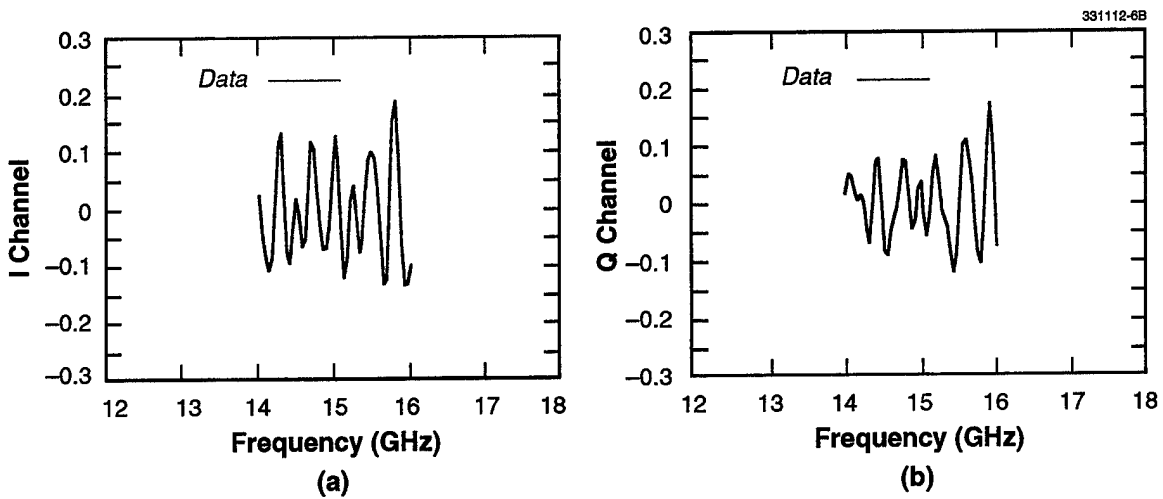


Figure 6. Static-range data of a monoconic target at 20-deg aspect for the (a) I channel and (b) Q channel.

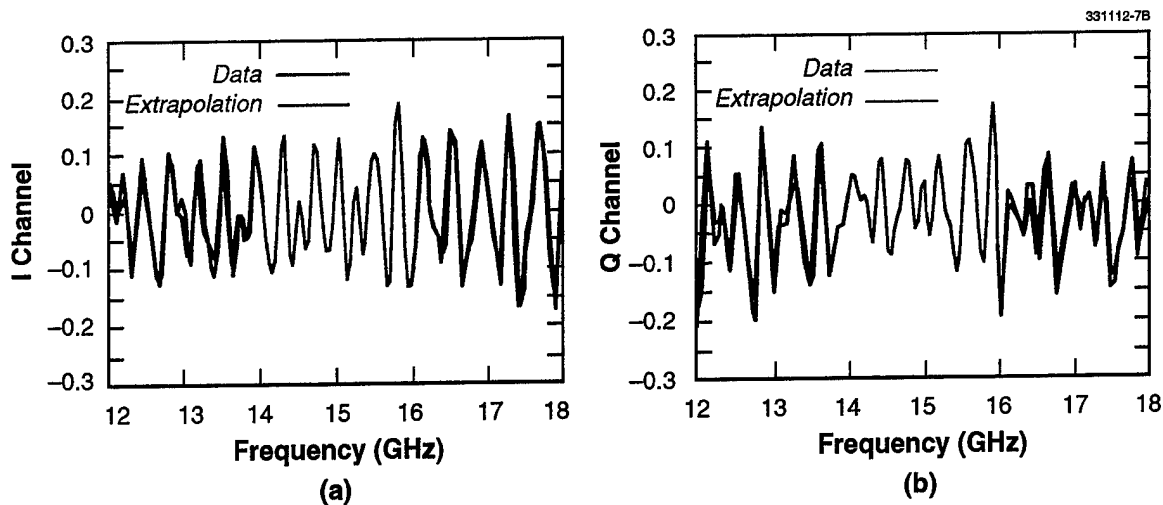


Figure 7. Comparison of the extrapolated data (blue) from a 2.0-GHz-wide (14.0 to 16.0 GHz) data set and the true data (red) for a monoconic reentry vehicle at 20-deg aspect for the (a) I channel and (b) Q channel.

Depending on the magnitude of the eigenvalues ($|\lambda|$), the extrapolation dies out for $|\lambda| < 1$ and increases rapidly for $|\lambda| > 1$ when the extrapolation factor is large. In the following example the state-space BWE processing technique is applied to a 1.0-GHz-wide subband data set in order to elucidate the limitations of BWE.

3.2.4 Example 4 (Static-Range Radar Data)

The radar pulse in the Example 3 was then reduced to a 1.0-GHz-wide data set in the range of 14.5 to 15.5 GHz. The state-space BWE technique is used to demonstrate the degradation of the predicted information for an extrapolation interval roughly three times the 1.0-GHz data subband on either side. Figures 8(a) and 8(b) compare the extrapolated model and the true full-band data for the I and Q channels, respectively. In these figures the extrapolated model grows in amplitude, and the extrapolation does not replicate the true data beyond a segment of 1.0-GHz on each side of the available data set.

The extrapolation may be sustained either by normalizing the eigenvalues (λ_i) or by providing data over a larger (perhaps sparse) band. If one normalizes the eigenvalues determined from the open-loop matrix A onto the unit circle, the extrapolated data clearly will not capture the exponential behavior of the embedded scattering centers; however, providing data over a second band (perhaps widely spaced) provides a much larger frequency span over which to estimate the frequency decay/growth. The additional band is also crucial to improving the accuracy of the α values. In the following sections a state-space technique is described that allows interpolation or extrapolation outside two mutually cohered subband measurements. The state-space method is formulated first.

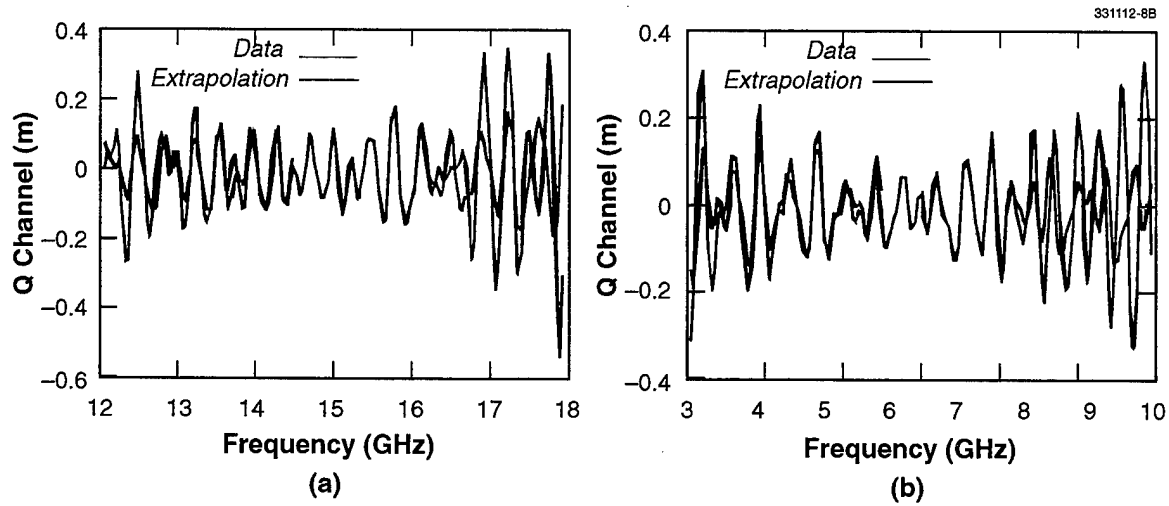


Figure 8. Comparison of the extrapolated data (blue) from a 1.0-GHz-wide (14.5 to 15.5 GHz) data set and true data (red) for the monoconic reentry vehicle at 20-deg aspect for the (a) I channel and (b) Q channel.

4. SPARSE-BAND STATE-SPACE FORMULATION

4.1 SPARSE-BAND REPRESENTATION

Suppose that two data sets are mutually coherent, i.e., that there are no phase and range biases between them as defined in [4]. Suppose also that the data set defined by Equation (28) in the frequency domain corresponds to the frequency response of the target over an arbitrary bandwidth. To generate the sparse-band measurements, let the first and last N_1 samples of the data be the entries of the first and second bands, respectively. Mathematically,

$$y_1 = [y(1) \ y(2) \ y(3) \ \dots \ y(N_1)] \quad (72)$$

and

$$y_2 = [y(N-N_1+1) \ y(N-N_1+2) \ y(N-N_1+3) \ \dots \ y(N)] \quad (73)$$

where N is the total number of samples, which is defined by Equation (28). An input-output description of the data set that includes y_1 , the data gaps, and the second data vector y_2 can be described by an ARMA model. A state-space formulation of this special data set may also be defined by Equations (8) and (9).

To estimate the missing samples and the target parameters buried in the data subsets, the state-space matrices (A , B , and C) must be computed. The next section presents a method to compute the state-space matrices for the UWB system described by Equations (8) and (9).

4.2 SPARSE-BAND IDENTIFICATION MATRICES

Suppose it is necessary to compute the state matrices for the sparse-band system described in the previous section. The following Hankel matrices may be formed from the data sets y_1 and y_2 :

$$H_1 = \begin{bmatrix} y(1) & y(2) & y(3) & \dots & y(L_1) \\ y(2) & y(3) & y(4) & \dots & y(L_1+1) \\ \cdot & \cdot & \cdot & \dots & \cdot \\ \cdot & \cdot & \cdot & \dots & \cdot \\ \cdot & \cdot & \cdot & \dots & \cdot \\ y(N_1-L_1) & y(N_1-L_1+1) & y(N_1-L_1+2) & \dots & y(N_1-1) \\ y(N_1-L_1+1) & y(N_1-L_1+2) & y(N_1-L_1+3) & \dots & y(N_1) \end{bmatrix} \quad (74)$$

and

$$H_2 = \begin{bmatrix} y(N-N_1+1) & y(N-N_1+2) & y(N-N_1+3) & \dots & y(N-N_1+L_1) \\ y(N-N_1+2) & y(N-N_1+3) & y(N-N_1+4) & \dots & y(N-N_1+L_1+1) \\ \vdots & \vdots & \vdots & \dots & \vdots \\ y(N-L_1) & y(N-L_1+1) & y(N-L_1+2) & \dots & y(N-1) \\ y(N-L_1+1) & y(N-L_1+2) & y(N-L_1+3) & \dots & y(N) \end{bmatrix}, \quad (75)$$

respectively. To achieve high resolution, the parameter L_1 , which denotes the correlation window length, is given by $(2N_1)/3$. To carry out the sparse-band state-space identification method, H_1 and H_2 must be stacked to form the dual-band Hankel matrix, H . Depending on the stacking method, a subaperture processing methodology is defined that provides the potential for robust parameter estimates from noisy data when H is given by

$$H = \begin{bmatrix} H_1 \\ H_2 \end{bmatrix}, \quad (76)$$

and an extended aperture processing is defined that provides the potential for true UWB resolution when H is defined by

$$H = [H_1 \ H_2]. \quad (77)$$

Because it has potential for the highest resolution, the extended aperture method described above will be used in this report, unless otherwise specified. A singular value decomposition carried out on H allows the separation of the noise from the signal space. By following the steps described in Section 2.4 for the single-band case, a p -rank approximation to the extended aperture H may also be defined by Equation (33). In this case $\tilde{\Omega}$ and $\tilde{\Gamma}$ denote the sparse-band observability and controllability matrices, respectively; thus, $\tilde{\Omega}$ and $\tilde{\Gamma}$ are defined by Equations (34) and (35), respectively. The sparse-band open-loop matrix A is obtained from the observability matrix $\tilde{\Omega}$ as defined by Equation (39). A may also be derived from the controllability matrix $\tilde{\Gamma}$. Using Equation (43) obtains, equivalently,

$$A = \tilde{\Gamma}_{-c1} \tilde{\Gamma}_{-cl}^* (\tilde{\Gamma}_{-cl} \tilde{\Gamma}_{-c1}^*)^{-1}, \quad (78)$$

where $\tilde{\Gamma}_{-c1}$ and $\tilde{\Gamma}_{-cl}$ are obtained by deleting the first and (L_1+1) -th columns and the L_1 -th and $2L_1$ -th columns of $\tilde{\Gamma}$, respectively. The state-space matrix C may be computed mathematically from Equation (44); however, to match the samples of the state-space impulse response to the corresponding sparse-band data points, B must be computed using a least-squares method. One way to compute B is to define a new observability matrix by

$$\tilde{\Omega}_N = \begin{bmatrix} C \\ CA \\ \cdot \\ \cdot \\ CA^{N_1-1} \\ CA^{N-N_1} \\ CA^{N-N_1+1} \\ \cdot \\ \cdot \\ CA^{N-1} \end{bmatrix}, \quad (79)$$

where N_1 and N are defined by Equations (72) and (73), respectively. The data sets y_1 and y_2 , together with $\tilde{\Omega}_N$, can be used in a least-squares sense to obtain

$$B = (\tilde{\Omega}_N^* \tilde{\Omega}_N)^{-1} \tilde{\Omega}_N^* [y_1 \ y_2]^T \quad (80)$$

It is not difficult to see that Equation (80) is identical to Equation (47). An expression that is analogous to B (which is defined above) may be derived for C . Equation (80) does not hold when computing C using a least-squares method. B must be computed from Equation (48). Next form a new controllability matrix $\tilde{\Gamma}_N$, which may be written as

$$\tilde{\Gamma}_N = \begin{bmatrix} B & AB & \dots & A^{N_1-1}B & A^{N-N_1}B & A^{N-N_1+1}B & \dots & A^{N-1}B \end{bmatrix} \quad (81)$$

The entries of $\tilde{\Gamma}_N$ as they are defined above are matrix elements; that is, when they are premultiplied by C their products can match the sparse-band data set in a least-squares sense. Finally, using Equation (51) obtains

$$C = [y_1 \ y_2] \tilde{\Gamma}_N^* (\tilde{\Gamma}_N \tilde{\Gamma}_N^*)^{-1} \quad (82)$$

The remarks made earlier regarding the single band also hold for the sparse band. When C is computed from the last equation, B must be derived from the controllability matrix $\tilde{\Gamma}$ as defined by Equation (48). Further, if C is given by Equation (44), B must be obtained from Equation (80). Thus for well-defined state-space matrices, the triplet (A , B , C) may be used to interpolate between the two bands and to extrapolate beyond, as well as to identify target features as described in Section 3.1 for the single-band case. The next section presents simulated and static-range radar data to test the feasibility of the UWB algorithm.

4.3 SIMULATED AND STATIC-RANGE EXAMPLES

To illustrate the limitations of the single-band processing technique and to confirm the UWB state-space technique, the simulated and static-range radar examples were repeated for the single-band case.

4.3.1 Example 5 (Simulated)

This example repeats the 200 independent trials of Example 2, which are now applied to sparsely located dual bands. For each trial the bandwidth of the synthetic pulse is reduced to two 1-GHz-wide bands spaced 5-GHz apart. Over the bands, the average for the I and Q channels for the 200 trials are shown in Figures 9(a) and 9(b), respectively.

Figures 10(a) and 10(b) compare the average of the lower subband using only the data for extrapolation and the full-band data sets for the I and Q channels, respectively. Because of the poor estimates of the signal parameters, particularly the α values over the limited bandwidth, the extrapolations shown in these figures do not mimic the true UWB channels. Table 4 gives the percentage error between the estimated and the true signal parameters.

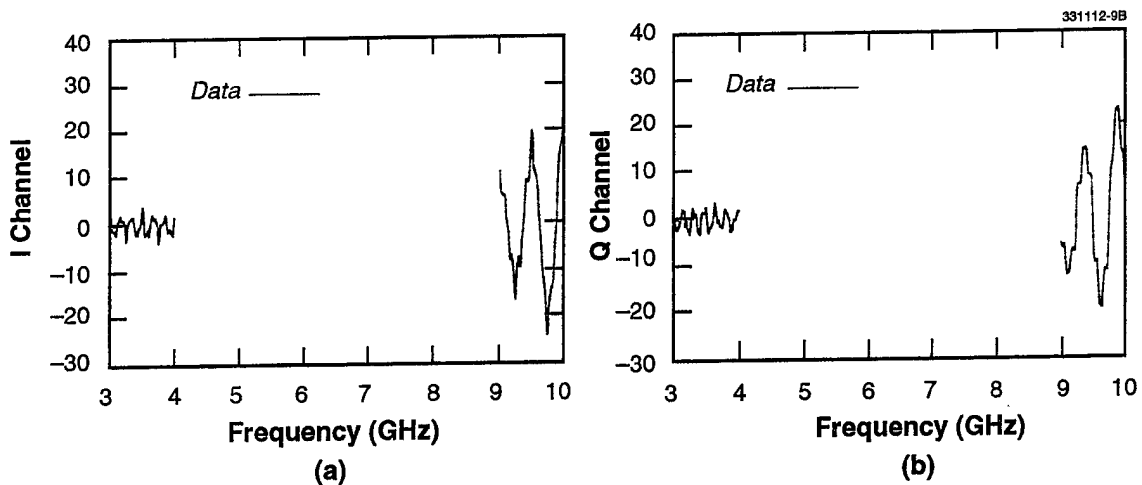


Figure 9. Average data samples for 200 independent trials of a four-point target with $SNR = 20$ dB for each run; (a) I channel, and (b) Q channel.

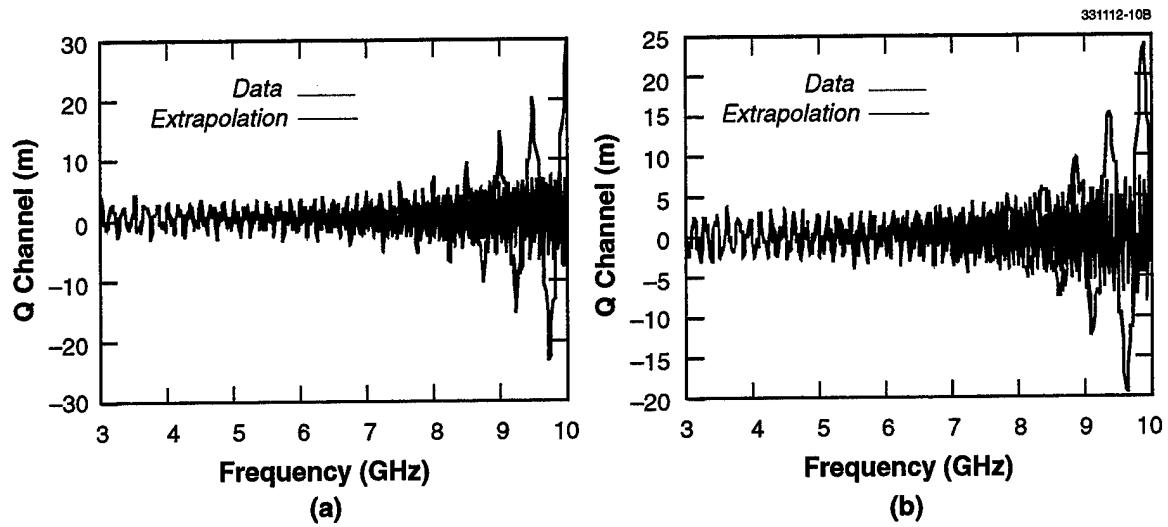


Figure 10. Comparison of the average of 200 independent trials for the lower-band extrapolations (blue) and truth data (red) for a four-point target with SNR = 40 dB for each run; (a) I channel, and (b) Q channel.

TABLE 4
Average Estimates of Signal Parameters Over 200 Trials Conducted
for Example 5, Lower-Band (SNR = 20 dB)

Scattering Centers	Decay/Growth (α)		Time Delay (τ)		Amplitude ($ a $)	
	Estimates	% Error	Estimates	% Error	Estimates	% Error
1st	-0.17×10^{-9}	81.6	14.01×10^{-9}	6.01	0.85	15.0
2nd	0.08×10^{-9}	65.34	5.95×10^{-9}	0.83	0.83	17.0
3rd	-0.1296×10^{-9}	57.88	1.04×10^{-8}	4.0	0.94	6.0
4th	13.34×10^{-9}	huge	15.68×10^{-9}	12.0	0.47	53.0

Conversely, Figures 11(a) and 11(b) show comparison using only the data from the upper-subband extrapolation and the UWB data sets for the I and Q channels, respectively. Over the full band the I and Q channels of the extrapolated and the true data match closely in magnitude, but not in phase. The deviations in phase of the extrapolations from the full-band channels is primarily because of error in the estimation of the time-delay parameters and the corresponding phases associated with the amplitudes of the scattering centers. Table 5 shows the percentage error between the estimated and true signal parameters.

Figure 12 illustrates the UWB sparse-band data fit using the state-space processing applied to the lower and upper bands. Parameter estimates are illustrated in Table 6. A comparison between Tables 1 and 6 reveals very good agreement between the estimates and the true signal parameters. Figures 12(a) and 12(b) show the excellent performance of the algorithm over the entire 7-GHz band for the average of the I and Q channels, respectively.

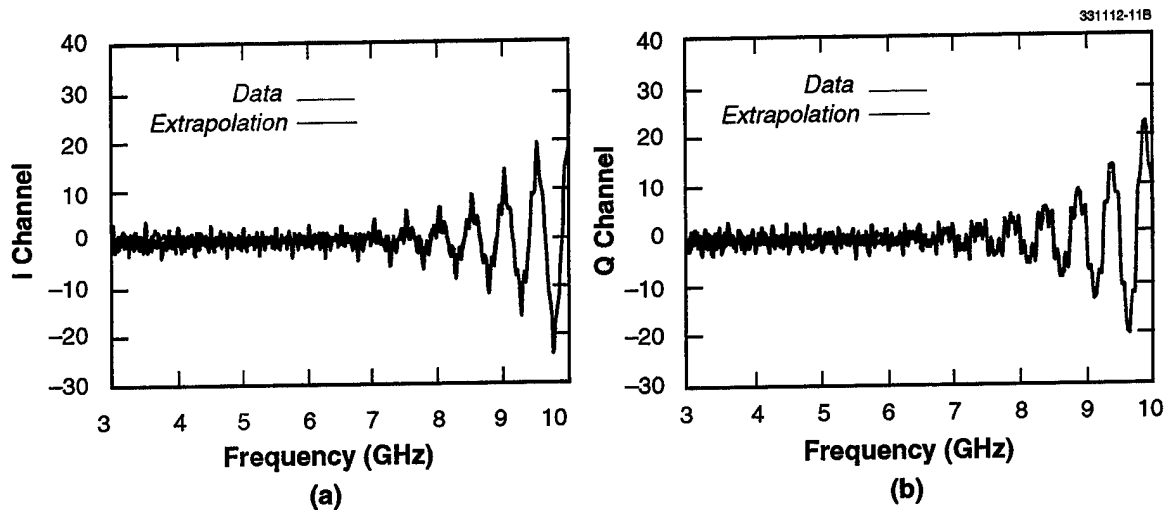


Figure 11. Comparison of the average of 200 independent trials for the upper-band extrapolations (blue) and truth data (red) for a four-point target with $SNR = 40$ dB for each run; (a) I channel, and (b) Q channel.

TABLE 5
Average Estimates of Signal Parameters Over 200 Trials Conducted
for Example 5, Upper-Band (SNR = 20 dB)

Scattering Centers	Decay/Growth (α)		Time Delay (τ)		Amplitude ($ a $)	
	Estimates	% Error	Estimates	% Error	Estimates	% Error
1st	-0.4104×10^{-9}	55.5	2.1×10^{-9}	5.0	0.927	7.3
2nd	-0.2667×10^{-9}	15.55	6.05×10^{-9}	0.83	1.13	13
3rd	-0.3723×10^{-9}	21.0	1.18×10^{-8}	18.0	1.08	8
4th	0.89×10^{-15}	88.0	13.87×10^{-9}	0.93	1.16	16

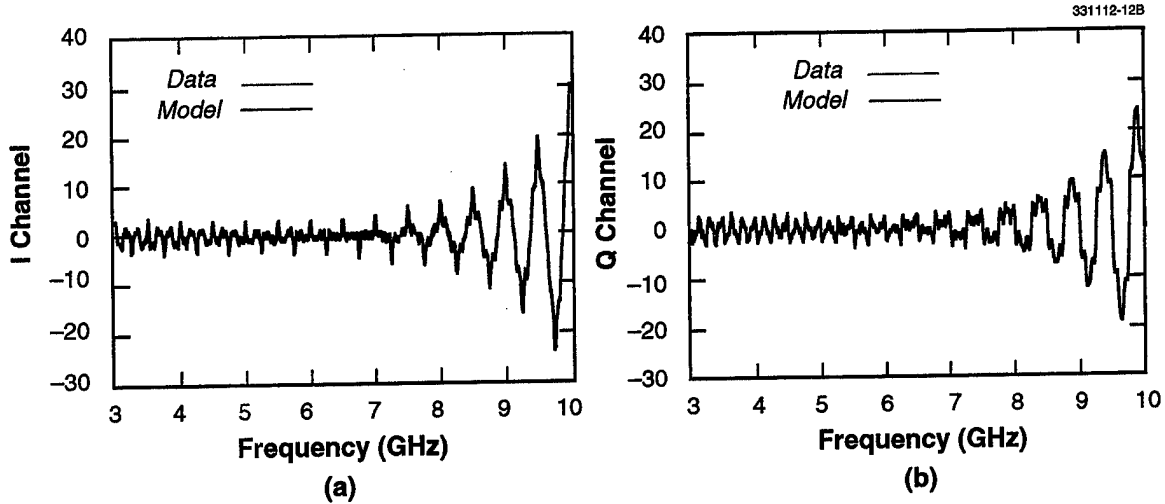


Figure 12. Comparison of the average of 200 independent trials of the UWB fitted model (blue) and truth data (red) for a four-point target with SNR = 20 dB for each run; (a) I channel, and (b) Q channel.

TABLE 6
Average Estimates of Signal Parameters over 200 Trials Conducted
for Example 5, Sparse-Band (SNR = 20 dB)

Scattering Centers	Decay/Growth (α)		Time Delay (τ)		Amplitude ($ a $)	
	Estimates	% Error	Estimates	% Error	Estimates	% Error
1st	-0.9193×10^{-9}	0.41	1.97×10^{-9}	1.5	0.95	5.0
2nd	-0.2281×10^{-9}	1.17	5.97×10^{-9}	0.5	1.05	5.0
3rd	-0.3273×10^{-9}	6.37	1.03×10^{-8}	3.0	0.97	3.0
4th	0.27×10^{-15}	1.7	14.02×10^{-9}	0.14	1.1	10.0

4.3.2 Example 6 (Simulated)

To test the feasibility of state-space UWB processing, the 200 independent trials of Example 1 were repeated, applied now to sparsely located dual bands. For each trial the bandwidth of the synthetic pulse was reduced to two 1-GHz-wide subbands 5-GHz apart. Figures 13(a) and 13(b) illustrate over the subbands the average of the data for the I and Q channels, respectively. Table 7 shows that the average estimates of the signal parameters match closely the entries of Table 1. Figures 14(a) and 14(b) show good agreement between the average of the predictions and the data for the I and Q channels, respectively.

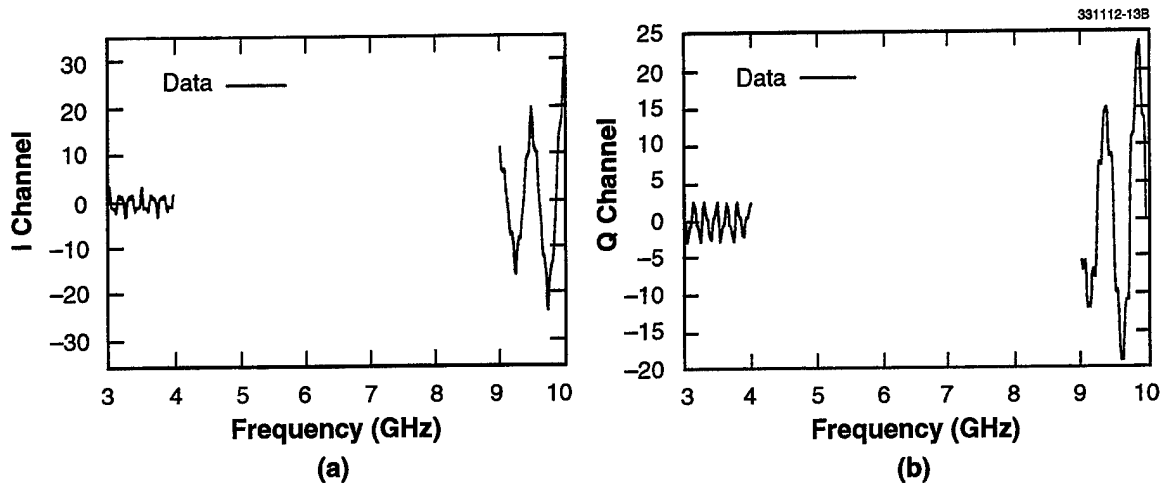


Figure 13. Average data samples for 200 independent trials of a four-point target with SNR = 40 dB for each run; (a) I channel and (b) Q channel.

TABLE 7

Average Estimates of Signal Parameters for 200 Trials Conducted
for Example 6, Sparse-Band (SNR = 40 dB)

Scattering Centers	Decay/Growth (α)		Time Delay (τ)		Amplitude ($ a $)	
	Estimates	% Error	Estimates	% Error	Estimates	% Error
1st	-0.9225×10^{-9}	0.07	2×10^{-9}	0	1.01	1.0
2nd	-0.2267×10^{-9}	1.78	6×10^{-9}	0	0.98	2.0
3rd	-0.3154×10^{-9}	2.50	1×10^{-8}	0	1.1	10.0
4th	0.36×10^{-14}	2.6	14×10^{-9}	0	1	0

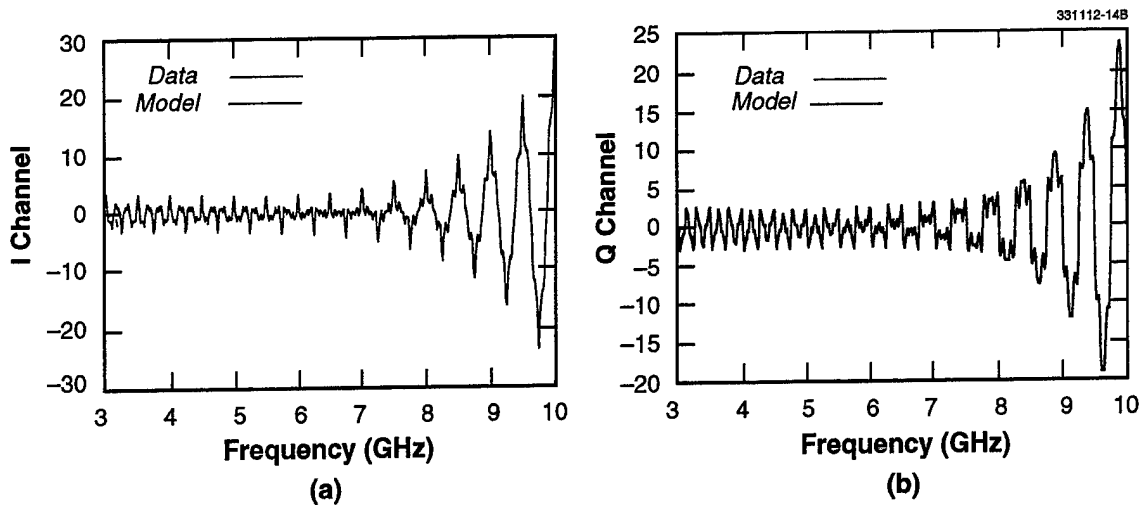


Figure 14. Comparison of the average of 200 independent trials of the UWB fitted model (blue) and truth data (red) for a four-point target with SNR = 40 dB for each run; (a) I channel (b) Q channel.

4.3.3 Example 7 (Static-Range Radar Data)

The static-range experiment of the monoconic target presented in Example 3 was considered in order to demonstrate the UWB state-space processing technique. The radar pulse was reduced to two 1-GHz-wide subbands, as illustrated in Figure 15(a). Figure 15(b) illustrates the compressed pulses for the two subbands, which are treated separately (i.e., 1-GHz resolution), and the full-band measurements. Most of the target features remain unresolved by the two subbands; the full-band compressed pulse resolves all the significant features on the target. Figure 16 illustrates the results of applying the sparse-band processing technique to the upper and lower data sets. Figure 16(a) shows good agreement between the data and the state-space interpolations and extrapolations. Figure 16(b) illustrates comparisons between the sparse-band target response and the true radar measurements. The model misses very few features on the target.

The last three examples show good performance with the state-space sparse-band processing using simulated and static-range radar data; however, enhanced performance can be achieved if the above results are used as initial conditions for an iterative algorithm, which fine-tunes the signal parameter estimates as defined by Equations (61), (62), and (66). Accordingly, the next section presents an iterative state-space UWB algorithm.

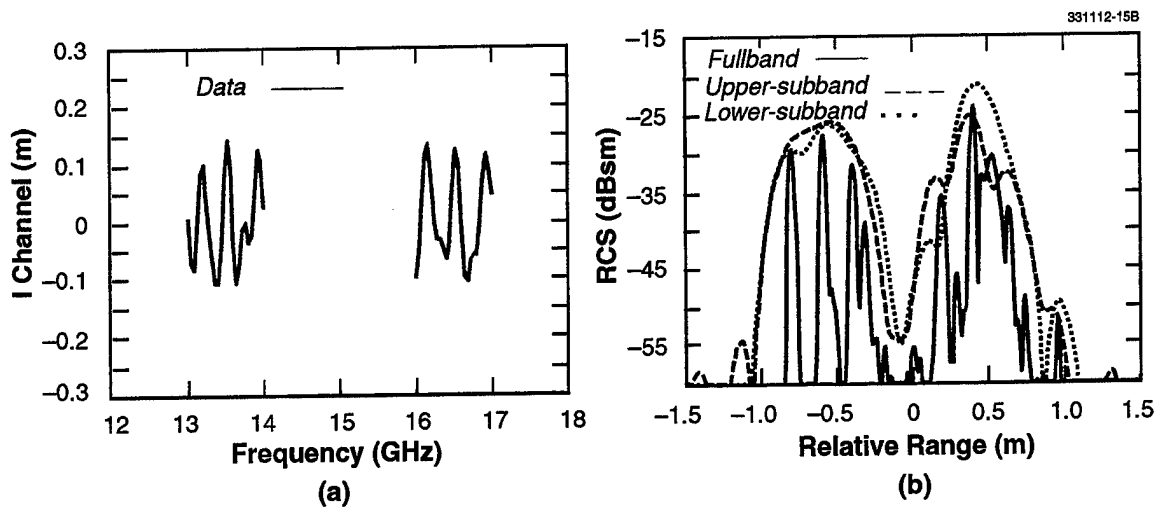


Figure 15. (a) Sparse-band measurements used to predict a monoconic reentry vehicle's response over the full band from 12 to 18 GHz. (b) Compressed pulses for the sparse- and full-band data sets.

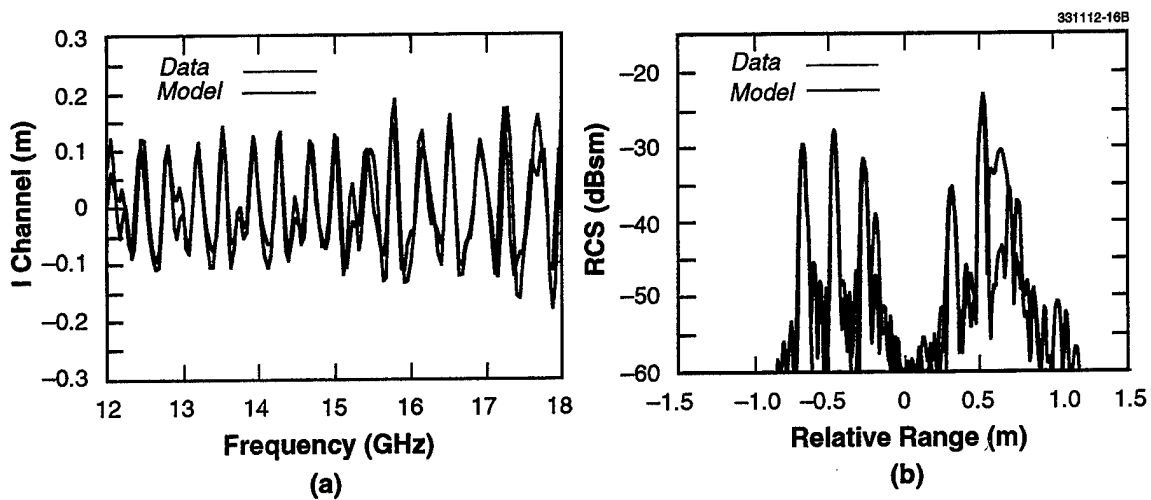


Figure 16. Comparison of full-band data (red) and the sparse-band model (blue) for a monoconic reentry vehicle at 20-deg aspect for the (a) I channel and (b) compressed pulses.

4.4 ITERATIVE METHOD FOR STATE-SPACE ESTIMATION AND INTERPOLATION

4.4.1 Method

This section presents an iterative approach that refines the state-space matrices of the dual band and improves the fitted data in the vacant bands. This iterative method uses the state-space matrices of the sparse-band algorithm as an initialization. At each step in the iteration, the algorithm evaluates the error energy between the measured and the estimated data in the lower and upper subbands. This error energy may be defined by

$$E = \sum_{k=1}^{N_1} |y_1(k) - \hat{y}_1(k)|^2 + \sum_{l=1}^{N_2} |y_2(l) - \hat{y}_2(l)|^2, \quad (83)$$

where $y_1(k)$ and $y_2(l)$ are the k th and l th samples of the first and second data sets, defined by Equations (72) and (73), respectively. Further, $\hat{y}_1(k)$ and $\hat{y}_2(l)$ denote the estimates of the measured samples $y_1(k)$ and $y_2(l)$, respectively. Using the measured data together with the initial estimate of the vacant band samples, the algorithm computes a new set of matrices based on the composite UWB data set (i.e., the full-band data set), generates a new fitted UWB data set, and calculates the error energy that is defined by Equation (83). The initial samples in the vacant bands and the UWB fitted data in the two subbands are then replaced by the new fitted samples and measurements. The algorithm updates the matrices, generates UWB fitted data, and computes a new error energy. During this procedure the new error energy is compared with the old one; as long as the new error energy is smaller than the previous error energy, the UWB algorithm repeats these steps iteratively. When the last computed error energy is greater than the previous one the algorithm stops, and the previous UWB fitted data thus define the so-called UWB synthetic pulse.

4.4.2 Example 8 (Static-Range Radar Data)

In order to estimate the target response more accurately, the sparse-band static-range example of UWB processing presented in Example 7 was repeated using the error-energy equation to obtain an enhanced fit to the full-band result. Figure 17(a) shows excellent agreement between the I channels of the data and the sparse-band model after eight iterations. The iterative UWB algorithm exhibits excellent performance. Figure 17(b) shows dramatic improvement in the target response from the slip-on ring (which cannot be seen in Figure 5) to the base edge. Figure 17 also illustrates that the algorithm's compressed pulse matches closely the true target response. Figure 18 shows that the locations of the eigenvalues of the open-loop matrix A are consistent with the physical scattering centers on the target. The eigenvalue corresponding to the nosetip response is close to the unit circle, indicating a nearly constant radar cross section (RCS) over the full band. The grooves and slip-on ring have nonconstant RCS as a function of frequency, as predicted by the moment-method RCS calculation illustrated in Figure 19. The corresponding eigenvalues are either inside or outside the unit circle, depending on whether the scatterer response is decaying or growing with frequency.

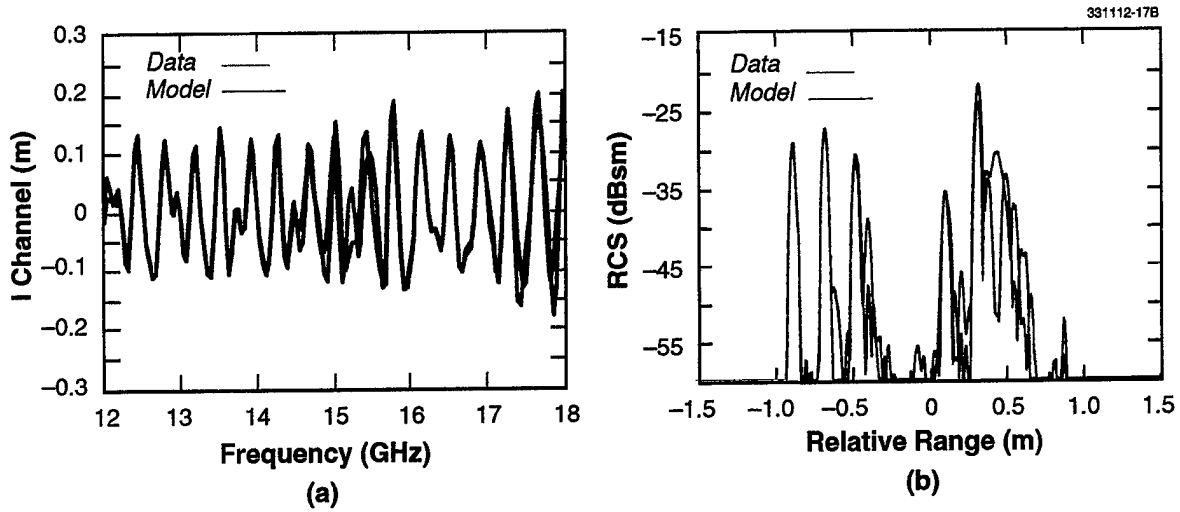


Figure 17. Comparison of the iterative UWB target response (blue) and full-band radar measurements (red) for a monoconic reentry vehicle at 20-deg aspect for the (a) I channel and (b) compressed pulses.

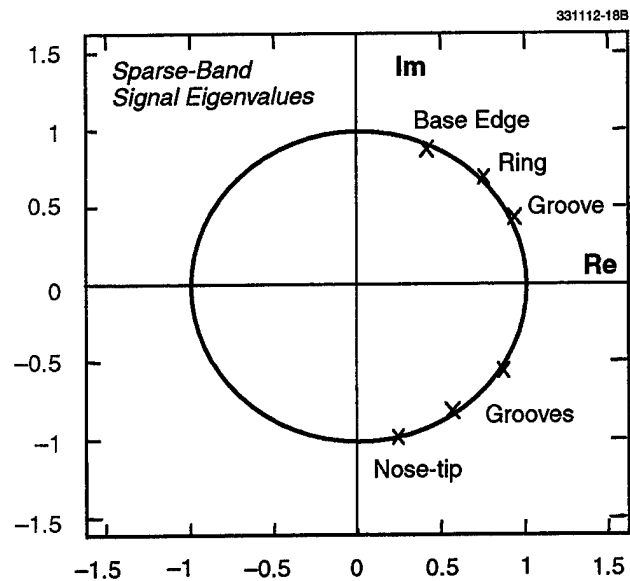


Figure 18. Iterative UWB eigenvalue estimates obtained using the sparse-band data sets illustrated in Figure 15(a).

The radar pulse in this example exhibits strong frequency-dependent behavior. The signal model of the scatterers on the monoconic target, instead of following Equation (1), follows the geometric theory of diffraction model as described in [8] and may be written as

$$y(k) = \sum_{i=1}^P a_i \left(\frac{f_k}{f_1}\right)^{\alpha_i} e^{-j2\pi\tau_k f_k + w(k)} \quad ; k = 1, \dots, N \quad (84)$$

The decay/growth for the major scattering centers can be computed indirectly using Equation (98); α_i may be obtained by matching the functions $(f_k/f_1)^{\alpha_i}$ and $|\lambda_i|^{k-1}$ at the highest extrapolated frequency. Mathematically,

$$\alpha_i = \frac{(N-1)\log(|\lambda_i|)}{\log\left[1 + (N-1)\frac{\Delta f}{f_1}\right]} \quad (85)$$

The above equation was used to estimate the decay/growth parameters for the first, second, and midbody grooves on the monoconic target to be $\alpha_1 = -1.1$, $\alpha_2 = 2.3$, and $\alpha_3 = 2.9$, respectively. These estimates are consistent with the moment-method RCS calculations shown in Figure 19.

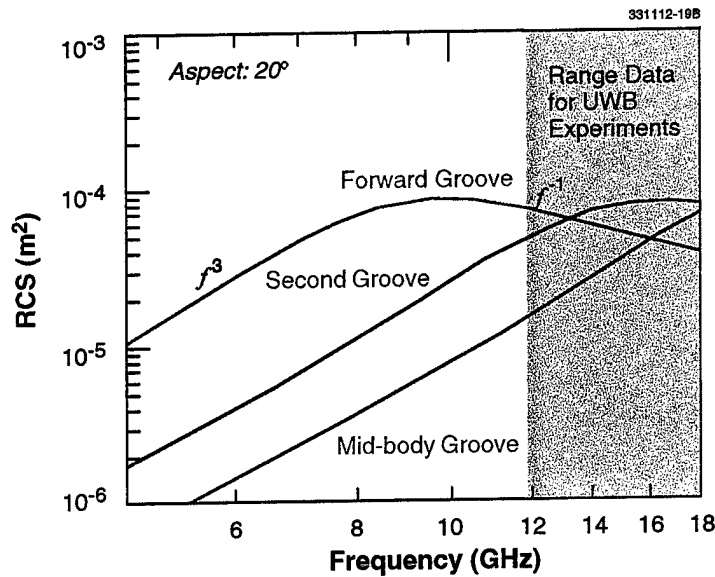
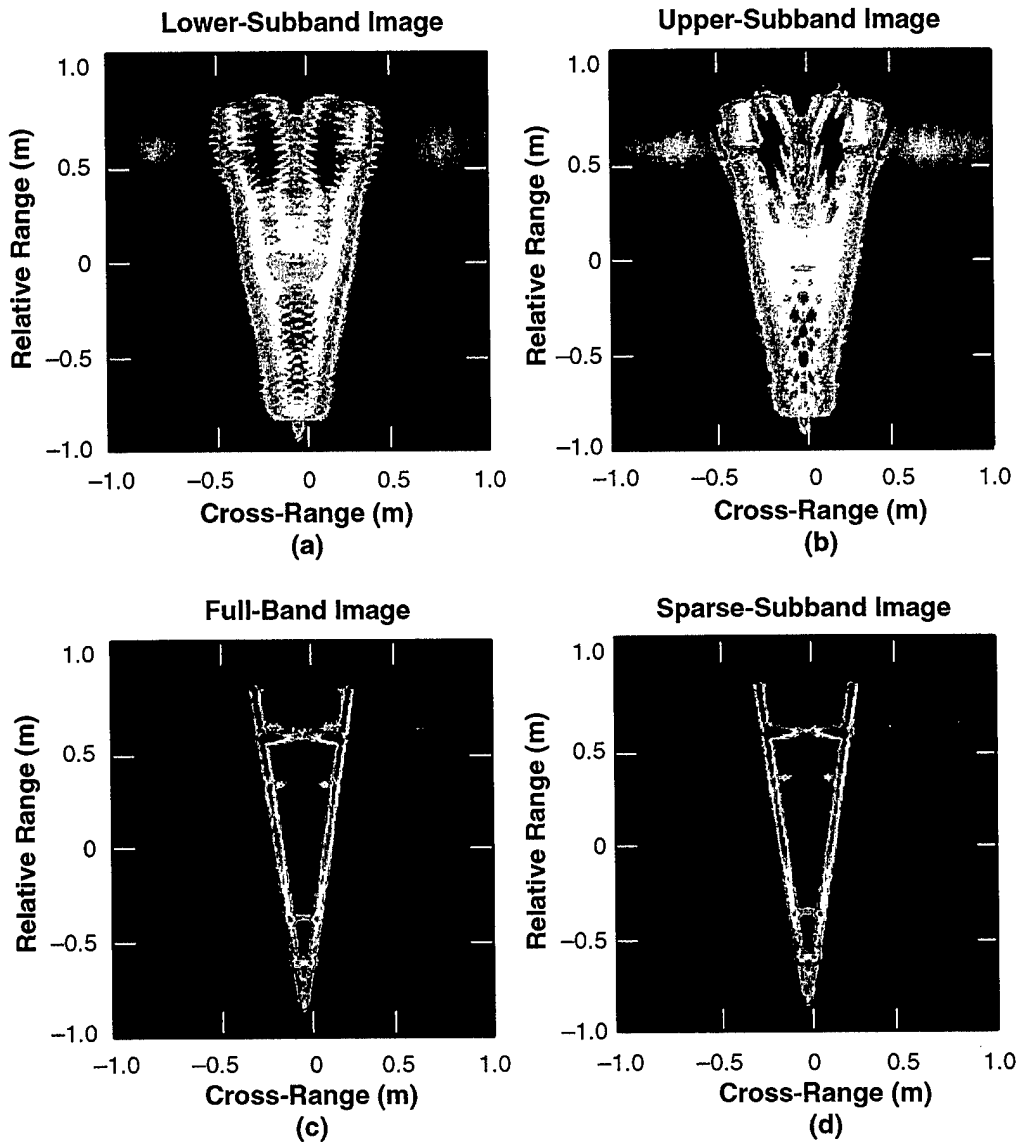


Figure 19. Moment-method RCS calculations for the three major grooves on the monoconic reentry vehicle, which was at a 20-deg aspect angle. All three grooves exhibit the expected f^3 scattering behavior at low frequencies, with breakpoints that depend on the size of the groove.

Because of the large viewing aspect of the target measurements, radar images of the target were generated. Figures 20(a) and 20(b) show the lower- and upper-subband images, respectively, using conventional imaging techniques. Given the relatively poor resolution of these images, the scattering centers on the target cannot be identified. Figures 20(c) and 20(d) show the true and the estimated sparse-band processing target images, respectively. The sparse-band image is comparable with the full-band image: it shows great detail of the target where the features are clearly identified. All four images were generated using extended coherent processing [9], and target symmetry was used to process the data as if a range of viewing aspects had been sampled from -95 to 95 deg.

331112-20B



Threshold: -50 dBsm

Figure 20. Comparison of two-dimensional radar images. The upper-left and -right images show the lower- and upper-subband images, respectively. The full-band image at the lower left uses actual radar measurements over the full 12-to-18-GHz frequency range. The sparse-band image in the lower right uses the sparse-band measurements with the iterative UWB prediction.

5. CONCLUSIONS

This report has presented a sparse-band state-space signal-processing technique to estimate signal parameters and predict data samples that lie outside the measurement band using simulated and static-range data. The technique has been applied to single- and sparse-band data samples. The algorithm provides more accurate estimates than previous algorithms of the time delay, decay/growth, and amplitude associated with each scatterer embedded in the data vectors. Extrapolation of the available data by a factor of three shows that the single-band state-space technique predicts well the outer-band samples; however, estimation of the frequency decay/growth parameter α is strongly sensitive to the available bandwidth. When applied to widely spaced sparse-band data samples, the technique provides a considerable improvement in estimating α . The technique also shows that accurate UWB radar returns can be achieved when only a few segments of the total UWB measurements are available. The technique is cost-effective, as it can compensate for the vacant bands when data are collected on restricted regions. Another advantage of the method is the accurate estimation of the decay/growth parameters, which provide the typing information for the scattering centers that characterize a target. The technique can be applied to many fields whenever the data are available in sparse subbands, as in a frequency jump burst radar or mutually cohered radars. For a well-defined signature fusion algorithm, the state-space UWB processing can be applied to radars that operate independently when the radars are properly cohered using the techniques described in [4].

REFERENCES

1. K.M. Cuomo, "A Bandwidth Extrapolation Technique for Improved Range Resolution of Coherent Radar Data," MIT Lincoln Laboratory, Lexington, Mass., Project Rep. CJP-60 Rev. 1 (4 December 1992). DTIC ADA-258462.
2. S.L. Borison, S.B. Bowling, and K.M. Cuomo, "Super-Resolution Method for Wideband Radar," *Lincoln Lab. J.*, 5, 441-461 (1992).
3. R. Carriere, "High Resolution Parametric Modeling of Canonical Radar Scatterers," Ph. D. thesis, The Ohio State University, (Cincinnati, Ohio), 1993.
4. K.M. Cuomo, J.E. Piou, and J.T. Mayhan, "Ultra-Wideband Coherent Processing" *IEEE Trans. Antennas and Propagation* (accepted for publication).
5. K. Ogata, *Discrete-Time Control Systems*, Englewood Cliffs, N.J.: Prentice-Hall, Inc. (1987).
6. U. B. Desai and D. Pal, "A Realization Approach to Stochastic Model Reduction and Balanced Stochastic Realizations," in *Proc. 21st IEEE Conf. Decision and Control*, IEEE, N.Y., N.Y. (1992), pp.1105-1112.
7. H. Akaike, "A New Look at the Statistical Model Identification," *IEEE Trans. Autom. Control*, 19, 716-723 (1974).
8. A. Moghaddar, Y. Ogawa, and E. K. Walton, "Estimating the Time-Delay and Frequency Decay Parameter of Scattering Components Using Weighted Subspace Smoothing," *IEEE Trans. Antennas Propag.*, 44, 179-187 (1996).
9. D.A. Ausherman et al., "Development in Radar Imaging," *IEEE Trans. Aerospace Electron.*, 20, 363-400 (1984).

REPORT DOCUMENTATION PAGE

Form Approved
OMB No. 0704-0188

Public reporting burden for this collection of information is estimated to average 1 hour per response, including the time for reviewing instructions, searching existing data sources, gathering and maintaining the data needed, and completing and reviewing the collection of information. Send comments regarding this burden estimate or any other aspect of this collection of information, including suggestions for reducing this burden, to Washington Headquarters Services, Directorate for Information Operations and Reports, 1215 Jefferson Davis Highway, Suite 1204, Arlington, VA 22202-4302, and to the Office of Management and Budget, Paperwork Reduction Project (0704-0188), Washington, DC 20503.

1. AGENCY USE ONLY (<i>Leave blank</i>)	2. REPORT DATE 20 July 1999	3. REPORT TYPE AND DATES COVERED Technical Report	
4. TITLE AND SUBTITLE A State-Space Technique for Ultrawide-Bandwidth Coherent Processing		5. FUNDING NUMBERS C — F19628-95-C-0002	
6. AUTHOR(S) Dr. Jean E. Piou, Dr. Kevin M. Cuomo, Dr. Joseph T. Mayhan		8. PERFORMING ORGANIZATION REPORT NUMBER TR-1054	
7. PERFORMING ORGANIZATION NAME(S) AND ADDRESS(ES) Lincoln Laboratory, MIT 244 Wood Street Lexington, MA 02420-9108		10. SPONSORING/MONITORING AGENCY REPORT NUMBER ESC-TR-98-066	
9. SPONSORING/MONITORING AGENCY NAME(S) AND ADDRESS(ES) U.S. Air Force, NAIC USASMDC Attn: DXDR Attn: SMDC-TC-SS 4180 Watson Way P.O. Box 1500 Wright-Patterson AFB, OH Huntsville, AL 35807-3801 45433-5648			
11. SUPPLEMENTARY NOTES None			
12a. DISTRIBUTION/AVAILABILITY STATEMENT Approved for public release; distribution is unlimited.		12b. DISTRIBUTION CODE	
13. ABSTRACT (<i>Maximum 200 words</i>) A scheme is presented for estimating the ultrawide-bandwidth position and typing of scattering centers on a target using sparse-band measurements. The algorithm determines a set of matrices that best describe the measured data, then the fitted data are used to interpolate between and extrapolate outside of the measurement bands. A modal decomposition approach is used to estimate the position and typing of the scatterers. Standard pulse-compression techniques are applied to obtain a highly defined range profile of the target; application of these techniques is followed by extended coherent processing to generate superresolved two-dimensional images. The effectiveness of the new algorithm is confirmed by computer simulations; it is tested further using static-range data on a canonical test object.			
14. SUBJECT TERMS		15. NUMBER OF PAGES 56	
		16. PRICE CODE	
17. SECURITY CLASSIFICATION OF REPORT Unclassified	18. SECURITY CLASSIFICATION OF THIS PAGE Unclassified	19. SECURITY CLASSIFICATION OF ABSTRACT Unclassified	20. LIMITATION OF ABSTRACT Same as Report